A SCALE-BRIDGING ANALYSIS FRAMEWORK FOR AN AIRCRAFT REAR FUSELAGE STRUCTURE WITH INTEGRATED ENGINES USING ISOGEOMETRIC ANALYSIS AND AUXETIC SANDWICH COMPOSITES

M. Friedrichs-Dachale*, N. Grünfelder†, M. Haupt*, T. Ricken†, S. Heimbs*

* Technische Universität Braunschweig, Institute of Aircraft Design and Lightweight Structures (IFL), Hermann-Blenk-Straße 35, 38108 Braunschweig, Germany

† University of Stuttgart, Institute of Statics and Dynamics of Aerospace Structures (ISD), Pfaffenwaldring 27, 70569 Stuttgart, Germany

Abstract

For future aircraft configurations, the integration of the engines into the rear fuselage for boundary layer ingestion redirects the load paths through the surrounding structure and introduces engine vibrations into the rear fuselage skin. Sandwich panels with an auxetic metamaterial core could be a promising concept for this region. Their material behavior can be tailored locally, while the auxetic core is reported to enhance energy dissipation and passive vibration damping. However, resolving the individual cells for a fuselage structure would lead to infeasibly large system sizes. This work therefore investigates an approach in which the resolved auxetic sandwich sections are replaced by a shell with homogenized stiffnesses. For this, a first-order computational homogenization of the core material is combined with classical laminate theory. The homogenized model is compared against a reference model with a resolved core under tension, shear and bending as well as in a modal analysis. The homogenized model reproduces the deformation modes of the resolved plate but is too compliant in all load cases, with deviations of up to 82% in the transverse strain response. The complete workflow is nevertheless demonstrated by assigning the homogenized stiffnesses to the inlet region of an isogeometric rear fuselage model under a $2.5\,$g pull-up maneuver. For quantitatively reliable results, an asymptotic homogenization of the complete sandwich section is proposed as the next step.

Keywords

Isogeometric analysis; auxetic structures; numerical homogenization; sandwich composites

NOMENCLATURE

Abbreviations

BLI	Boundary Layer Ingestion
CAD	Computer-Aided Design
CLT	Classical Laminate Theory
DOF	Degree of Freedom
IGA	Isogeometric Analysis
RVE	Representative Volume Element

1. INTRODUCTION AND MOTIVATION

A promising concept for reducing the fuel consumption of future transport aircraft is boundary layer ingestion (BLI). When the engines are embedded into the fuselage, the boundary layer forming on it is ingested into the engine, which can reduce the wake drag and improve the overall efficiency of the aircraft [1, 2]. However, from an aerodynamic perspective the engine and the airframe can no longer be treated independently. The engine inlet no longer receives a clean free stream but the distorted boundary layer of the fuselage, whose state changes considerably over the flight envelope and can provoke flow separation in different regions of the intake [3]. From a structural perspective, the skin around the inlet has to carry the loads from the integrated engines through the rear fuselage, while minimizing the cabin noise and the vibrations resulting from the engine integration.

A possible way to meet these requirements is the use of auxetic metamaterials, which are engineered cellular structures with a negative Poisson's ratio. Their deformation is determined not by the base material but by their cell geometry. When used as a sandwich core, such cells interact with the non-auxetic face sheets, so that energy is stored and dissipated more effectively than in a conventional sandwich structure [4, 5]. This behavior has been exploited for enhanced energy dissipation [6], high energy absorption [7] and passive vibration damping [8]. Since the response results from the cell geometry, it can be precisely tuned

CC BY 4.0

doi: 10.25967/680369

locally through the deformation mechanism of the cell [9], without altering the base material.
In BLI configurations, such sandwich structures incorporating an auxetic material could be used in the inlet region, as the face sheets provide a smooth surface for flow guidance while maintaining the tailored mechanical behavior beneath. Beyond this passive behavior, auxetic materials also open up the possibility of deformable surfaces [10], which can offer significant advantages for flow characteristics [11], and they provide stabilizing effects on curved and doubly curved surfaces [12].
Despite these advantages, significant challenges still prevent the widespread use of auxetic metamaterials in aerospace applications, since achieving the beneficial properties in practice requires extensive numerical modeling. For components of the size of the proposed inlet region, the complex cell geometry leads to systems with a high number of degrees of freedom. The unit cells are smaller than the macroscopic component by multiple orders of magnitude, making it prohibitively expensive to resolve their fine details. Many auxetic structures additionally feature notches, which further increase the modeling effort and the complexity.
Recently, numerous approaches have been proposed on how to reduce the computational effort associated with such structures without compromising the accuracy required to analyze the detailed properties described above. Notable examples include methods for reducing the fidelity of the models [13], several approaches involving machine learning [14], asymptotic homogenization [15] and two-scale computational homogenization [16].
The present work performs a homogenization of a sandwich material with an auxetic core in order to make use of the advantages listed above while keeping the analysis on the macroscale computationally feasible (see Fig. 1). At the mesoscale, the ABD matrix of the sandwich material with an auxetic core is obtained using a first-order computational homogenization of the core in combination with classical laminate theory. It is compared against a resolved reference model under tensile, shear and bending loads as well as in a modal analysis. At the macroscale, the rear fuselage is modeled using isogeometric analysis (IGA), which allows the structural analysis to be performed directly on the CAD description of the fuselage geometry. The homogenized stiffness can then be assigned to the skin of the inlet region, so that the core topology becomes a design variable at fuselage structural component scale.

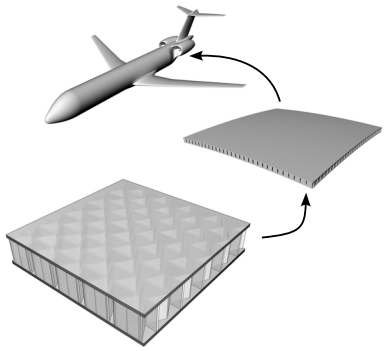


FIG 1. Overview of the intended scale-bridging analysis framework.

1.1. Mesoscale: Sandwich with Auxetic Core and Reference Unit Cell

For the following investigations, a re-entrant auxetic cell is chosen as the representative unit cell. Its geometry is deliberately kept simple and essentially corresponds to a honeycomb structure with inverted diagonal struts. The auxetic effect results from the re-entrant angle α of the diagonal struts (see Fig. 2). The corresponding dimensions are listed in Tab. 1 and Fig. 2, where w and h denote the total width and height of a cell, H its depth, and t the strut thickness. The core material is steel (EN 1.4310, $E = 185\,\mathrm{GPa}$, $\nu = 0.30$, $\rho = 7.9\,\mathrm{g/cm^3}$), while the face sheets are quasi-isotropic S2-glass/epoxy laminates ($[45/-45/0/90]_s$) with a ply thickness of 0.125 mm [17, Tab. 1]. The $0°$ ply is oriented along the x-axis of the auxetic cell.

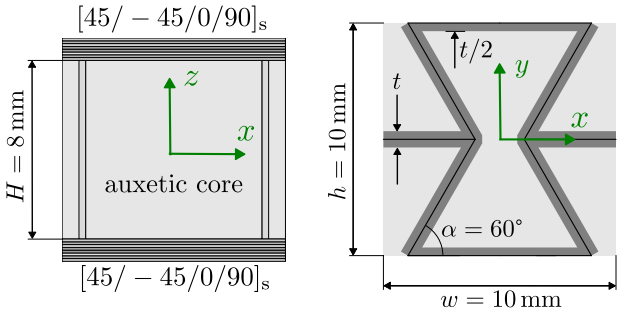


FIG 2. Dimensions of sandwich with a re-entrant auxetic core.

TAB 1. Geometry parameters of one auxetic re-entrant unit cell.

w	h	H	α	t
in mm	in mm	in mm	in °	in mm
10	10	8	60	0.7

1.2. Macroscale: Structural Design Using Isogeometric Analysis

On the macroscale, the aim is to find unconventional stiffening topologies that minimize the structural

CC BY 4.0

weight of the rear fuselage. Isogeometric analysis (IGA) is used for this purpose. IGA uses the functions that describe the geometry, in this case NURBS, as basis functions for the structural analysis [18]. Geometry and simulation model are therefore no longer two separate representations. Instead, the CAD description of the outer fuselage shape is the analysis model itself, so that the meshing step and the geometric approximation it introduces are avoided [19]. Refinement reduces to knot insertion or degree elevation on that same description, which keeps the geometry exact at every refinement level and gives a high solution accuracy with comparatively few degrees of freedom. Since the basis functions are up to C^{p-1}-continuous across element boundaries, element formulations with continuity requirements beyond C^0 become accessible. In the following homogenized simulations a Kirchhoff–Love shell is used, which is not directly accessible with C^0 Lagrange elements.

A further advantage of using IGA is the possibility of modeling the fuselage reinforcing elements as beams embedded into the fuselage shell, as proposed by Bauer et al. [20]. For the fuselage structural design, the stringer layouts are described as curves in the parameter space of the fuselage shell and mapped into physical space, so that the stiffeners introduce no degrees of freedom of their own. Instead, their structural response is expressed entirely through the shell. The stiffener layout is thereby decoupled from the shell discretization so that a stiffener can be moved, added or removed without re-meshing, and the shell discretization does not have to follow the stiffening layout. Together with the direct use of the CAD geometry, this makes the approach well suited for the early design stage, where the outer fuselage shape, the position of the integrated engines and the stiffening layout all change from one variant to the next.

2. HOMOGENIZATION APPROACH

This section presents the homogenization approach used to apply the advantages of auxetic materials from the mesoscale (see Sec. 1.1) to the macroscale (see Sec. 1.2). The approach consists of two steps. First, the material properties of the auxetic sandwich core are determined on a unit cell, using first-order computational homogenization. Thereafter, the ABD-matrix of the shell is calculated using classical laminate theory (CLT) by integrating the layer stiffnesses through the thickness.

2.1. Computational Homogenization of a Periodic Unit Cell

The goal of homogenization is to replace the periodic mesostructure, in this case the auxetic sandwich core, by an equivalent homogeneous medium that reflects the cell-averaged stiffness and deformation behavior. For this, the displacement field of a representative volume element (RVE) is split into a linear macroscopic part and a periodic fluctuation, $\mathbf{u}(\mathbf{x}) = \bar{\boldsymbol{\varepsilon}}\,\mathbf{x} + \tilde{\mathbf{u}}(\mathbf{x})$, where the fluctuation $\tilde{\mathbf{u}}$ takes the same value at any two opposite boundary points. Since the cell walls are prismatic in the z-direction, the RVE does not have to span the full depth H, but a slice of height $\bar{H} = H/4$ is used instead. The opposite boundaries are separated by w, h or $\bar{H}$ in the x-, y- or z-direction, collected in the period vector $\mathbf{p}$. Subtracting the displacements of such a boundary pair therefore cancels the fluctuation and leaves

$$\mathbf{u}(\mathbf{x}+\mathbf{p}) - \mathbf{u}(\mathbf{x}) = \bar{\boldsymbol{\varepsilon}}\,\mathbf{p}. \tag{1}$$

Consequently, the relative displacement of every boundary pair is prescribed by the macroscopic strain tensor $\bar{\boldsymbol{\varepsilon}}$ and the cell dimensions alone, independent of the position $\mathbf{x}$ on the face. The three resulting offsets are stored in one reference point per direction, RP_x, RP_y and RP_z, and enforced by linear constraint equations between each dependent node d and its independent periodic image n on the opposite face. This leads to the following equations

$$\begin{aligned} u_i^{d_x} - u_i^{n_x} - U_i^x &= 0, \\ u_i^{d_y} - u_i^{n_y} - U_i^y &= 0, \qquad i = 1,2,3, \\ u_i^{d_z} - u_i^{n_z} - U_i^z &= 0, \end{aligned} \tag{2}$$

with the reference-point displacements holding the columns of the macroscopic strain tensor scaled by the respective cell period,

$$\begin{aligned} \mathbf{U}^x = \bar{\boldsymbol{\varepsilon}} \begin{pmatrix} w \\ 0 \\ 0 \end{pmatrix}, \; \mathbf{U}^y = \bar{\boldsymbol{\varepsilon}} \begin{pmatrix} 0 \\ h \\ 0 \end{pmatrix}, \; \mathbf{U}^z = \bar{\boldsymbol{\varepsilon}} \begin{pmatrix} 0 \\ 0 \\ \bar{H} \end{pmatrix}, \\ \bar{\boldsymbol{\varepsilon}} = \begin{pmatrix} \bar{\varepsilon}_{11} & \frac{1}{2}\bar{\gamma}_{12} & \frac{1}{2}\bar{\gamma}_{13} \\ \frac{1}{2}\bar{\gamma}_{12} & \bar{\varepsilon}_{22} & \frac{1}{2}\bar{\gamma}_{23} \\ \frac{1}{2}\bar{\gamma}_{13} & \frac{1}{2}\bar{\gamma}_{23} & \bar{\varepsilon}_{33} \end{pmatrix}. \end{aligned} \tag{3}$$

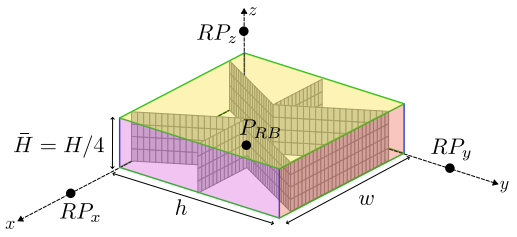


FIG 3. Application of the periodic boundary conditions for the RVE.

Because the cell walls are discretized with shell elements, the rotations must be periodic as well. Since there is no macroscopic strain gradient in first-order homogenization, the rotational fluctuation is periodic and the jump disappears entirely. For the pairs of opposite faces the constraints read

CC BY 4.0

$$
\begin{aligned}
\theta_i^{d_x} - \theta_i^{n_x} &= 0, \\
\theta_i^{d_y} - \theta_i^{n_y} &= 0, \qquad i = 4, 5, 6. \\
\theta_i^{d_z} - \theta_i^{n_z} &= 0,
\end{aligned} \tag{4}
$$

The green and blue edges in Fig. 3 belong to two face pairs simultaneously, so nodes belonging to these edges are paired in one direction only. Furthermore, one interior node P_{RB} is fixed to remove the rigid-body translation. To compute the material properties, three tension and three shear load cases are applied, which are listed in Tab. 2. The reaction force (RF) at a reference point equals the resultant force transmitted across the corresponding cell face, and the enclosing surface areas of the RVE are $A_x = h\bar{H}$, $A_y = w\bar{H}$ and $A_z = wh$.

TAB 2. Boundary conditions in the RVE model for the six individual load cases. The in-plane cell dimensions w and h are listed in Tab. 1, $\bar{H} = H/4$ is the RVE height.

DOF	Tension			Shear		
	x	y	z	xy	xz	yz
Interior Node (Suppressing Rigid Body Movement)						
u_1	0	0	0	0	0	0
u_2	0	0	0	0	0	0
u_3	0	0	0	0	0	0
RP_x						
u_1	w	free	free	0	0	0
u_2	0	0	0	$w/2$	0	0
u_3	0	0	0	0	$w/2$	0
RP_y						
u_1	0	0	0	$h/2$	0	0
u_2	free	h	free	0	0	0
u_3	0	0	0	0	0	$h/2$
RP_z						
u_1	0	0	0	0	$\bar{H}/2$	0
u_2	0	0	0	0	0	$\bar{H}/2$
u_3	free	free	$\bar{H}$	0	0	0

Uniaxial tension in x is imposed by prescribing $U_1^x = w$, which corresponds to a unit strain $\bar{\varepsilon}_{11} = 1$. The reference points RP_y and RP_z are left unloaded and free, so that the cell can contract freely in the transverse direction. The Young's modulus and the Poisson's ratios then follow from the effective stresses and the respective strains, illustrated using the example of $\bar{\sigma}_{11}$ and all strain components as follows:

$$
\begin{aligned}
\bar{\sigma}_{11} &= \frac{\mathrm{RF}_1^x}{A_x}, \quad \bar{\varepsilon}_{11} = \frac{U_1^x}{w}, \\
\bar{\varepsilon}_{22} &= \frac{U_2^y}{h}, \quad \bar{\varepsilon}_{33} = \frac{U_3^z}{\bar{H}}.
\end{aligned} \tag{5}
$$

From these relations, the Young's modulus E_1 and the two Poisson's ratio components ν_{12} and ν_{13} can be calculated as follows:

$$
E_1 = \frac{\bar{\sigma}_{11}}{\bar{\varepsilon}_{11}}, \quad \nu_{12} = -\frac{\bar{\varepsilon}_{22}}{\bar{\varepsilon}_{11}}, \quad \nu_{13} = -\frac{\bar{\varepsilon}_{33}}{\bar{\varepsilon}_{11}}. \tag{6}
$$

Tension in y and z is applied in the same manner and yields E_2, ν_{21}, ν_{23}, as well as E_3, ν_{31}, ν_{32}. For the shear cases the strain jump is introduced at two reference points simultaneously. For shear in the x-y-plane, this leads to $U_2^x = \frac{1}{2}\,w$ and $U_1^y = \frac{1}{2}\,h$. The shear stress is then available from either reference point,

$$
\begin{aligned}
\bar{\tau}_{12} &= \frac{\mathrm{RF}_1^y}{A_y} = \frac{\mathrm{RF}_2^x}{A_x}, \\
\bar{\gamma}_{12} &= \frac{U_2^x}{w} + \frac{U_1^y}{h}, \quad G_{12} = \frac{\bar{\tau}_{12}}{\bar{\gamma}_{12}}.
\end{aligned} \tag{7}
$$

The remaining shear moduli follow analogously as

$$
G_{13} = \frac{\mathrm{RF}_1^z/A_z}{U_3^x/w + U_1^z/\bar{H}}, \qquad G_{23} = \frac{\mathrm{RF}_2^z/A_z}{U_3^y/h + U_2^z/\bar{H}}. \tag{8}
$$

2.2. Computation of the ABD Matrix

The homogenized core is now treated as one thick ply in the composite stack. Its orthotropic constants are the RVE results computed in the previous section. The ABD matrices used for the isogeometric shell model are now computed according to classical laminate theory, which was implemented in the IGA solver of Kratos Multiphysics [19, 21]. For each layer k the reduced plane-stress stiffness is computed as

$$
\mathbf{Q}^{(k)} = \begin{pmatrix} \dfrac{E_1}{1-\nu_{12}\nu_{21}} & \dfrac{\nu_{12}E_2}{1-\nu_{12}\nu_{21}} & 0 \\ \dfrac{\nu_{12}E_2}{1-\nu_{12}\nu_{21}} & \dfrac{E_2}{1-\nu_{12}\nu_{21}} & 0 \\ 0 & 0 & G_{12} \end{pmatrix}. \tag{9}
$$

The reduced plane-stress stiffness matrix is then rotated by the ply angle φ_k with the transformation matrix $\mathbf{T}_\varepsilon$.

$$
\bar{\mathbf{Q}}^{(k)} = \mathbf{T}_\varepsilon^T(\varphi_k)\,\mathbf{Q}^{(k)}\,\mathbf{T}_\varepsilon(\varphi_k). \tag{10}
$$

To compute the ABD matrix, the rotated matrices are integrated over the through-thickness coordinates z_{k-1}, z_k of the layer boundaries, measured from the laminate midplane.

$$
\begin{aligned}
\mathbf{A} &= \sum_k \bar{\mathbf{Q}}^{(k)}\,(z_k - z_{k-1}), \\
\mathbf{B} &= \tfrac{1}{2}\sum_k \bar{\mathbf{Q}}^{(k)}\,(z_k^2 - z_{k-1}^2), \\
\mathbf{D} &= \tfrac{1}{3}\sum_k \bar{\mathbf{Q}}^{(k)}\,(z_k^3 - z_{k-1}^3).
\end{aligned} \tag{11}
$$

CC BY 4.0

Although the approach is simple to implement, it is based on assumptions that the real sandwich does not satisfy. First, the continuum assumption requires the cell to be small compared to the region it fills. Second, classical laminate theory reduces every layer to a plane stress state, so that only E_1, E_2, ν_{12} and G_{12} enter the reduced stiffness $\mathbf{Q}^{(k)}$, while E_3, ν_{13}, ν_{23}, G_{13} and G_{23} are discarded. An alternative approach to calculating the ABD matrix that avoids these problems is asymptotic homogenization, which will be investigated in future work.

2.3. Homogenization of the Mass

The modal analysis in Sec. 3 additionally requires the inertia of the section. Unlike the stiffness, it requires no cell problem, since the kinetic energy is treated as a plain volume average. The effective core density is the density of the wall material scaled by the relative density of the cell, $\rho^* = \rho_{\mathrm{rel}}\,\rho_{\mathrm{wall}}$, and the core becomes one further homogeneous layer of the section. The relevant quantity for a shell is the mass per unit area,

$$I_0 = \int \rho \,\mathrm{d}z = \sum_k t_k\,\rho_k, \tag{12}$$

where the density ρ is integrated along the thickness coordinate z. This reduces to the sum of thickness t_k times density ρ_k over the layers k of the section.

3. COMPARISON AT PANEL LEVEL

3.1. Resulting ABD Matrix

First, the ABD matrix resulting from the homogenization approach of Sec. 2.1 is computed. For the homogenized auxetic core, the method yields $E_1 = 436.4\,\mathrm{MPa}$, $E_2 = 1324.4\,\mathrm{MPa}$, $G_{12} = 50.4\,\mathrm{MPa}$, $\nu_{12} = -0.540$ and $\nu_{21} = -1.637$. The reduced plane-stress stiffness computed from these constants with Eq. (9) is then inserted into the CLT routine of the IGA code as an additional core layer between the two face laminates, which results in a stack of 17 layers. The ABD matrix that follows from Eq. (11) is shown in Fig. 4. The entries of $\mathbf{A}$ are given in MN/m and those of $\mathbf{D}$ in N m. As expected for a symmetric layup, the $\mathbf{B}$ matrix is zero.

	ε_{11}	ε_{22}	γ_{12}	κ_{11}	κ_{22}	κ_{12}
N_{11}	94.6	-28.5	0.00	0	0	0
N_{22}	-28.5	155.5	0.00	0	0	0
N_{12}	0.00	0.00	22.5	0	0	0
M_{11}	0	0	0	1475	156	0.4
M_{22}	0	0	0	156	1799	0.4
M_{12}	0	0	0	0.4	0.4	452

FIG 4. ABD matrix of the sandwich section obtained with the RVE homogenization combined with CLT.

In the following, the resolved model is compared with the homogenized model for several load cases.

3.2. Square Plate under Different Load Cases

3.2.1. Axial Tension

As a first example, a $500\,\mathrm{mm} \times 500\,\mathrm{mm}$ plate under a uniaxial tension of $N_{11} = 200\,\mathrm{N/mm}$ is considered, where the 0°-layers are oriented along the x-axis. The resolved model was analyzed with Abaqus using S4 shell elements and $7\,083\,614$ degrees of freedom. The axial resultant is introduced as a force of $F = 100\,\mathrm{kN}$ on a reference point that is tied to all nodes of the loaded end cross-section by linear constraint equations, so that this end remains plane. The opposite end is tied to a second reference point held at $u_x = 0$. Additionally, three pins on the outer face remove the rigid-body motion.
The homogenized model was analyzed using isogeometric Kirchhoff–Love shell elements with three translational degrees of freedom per control point. The mesh of 5×5 control points results in 75 degrees of freedom. The IGA model introduces the same resultant as a line load on one end control point row and keeps the ends plane by multi-point constraints. One point on the edge opposite the loaded edge is constrained in all three translations, and two further points are constrained in the z-direction to remove the rigid-body motion.
Fig. 5 shows the displacement field on the top surface of the resolved plate (a), compared with the IGA result obtained with the ABD matrix from the first-order computational homogenization (b). It can be seen that the first-order homogenization results are too compliant and overestimate the auxetic behavior. The same is observed in the comparison of the axial and lateral strains in Tab. 3, where the effective strains were evaluated from the edge-averaged displacements $\langle\,\cdot\,\rangle$ as

CC BY 4.0

$$\bar{\varepsilon}_{xx} = \frac{\langle u_x \rangle_{x=L_x} - \langle u_x \rangle_{x=0}}{L_x},$$
$$\bar{\varepsilon}_{yy} = \frac{\langle u_y \rangle_{y=L_y} - \langle u_y \rangle_{y=0}}{L_y}, \tag{13}$$
$$\nu_{\text{eff}} = -\frac{\bar{\varepsilon}_{yy}}{\bar{\varepsilon}_{xx}},$$

with the plate edge lengths $L_x = L_y = 500\,\text{mm}$.

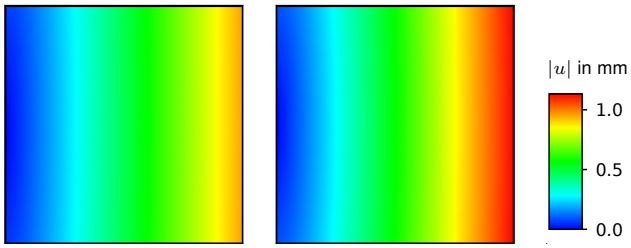


FIG 5. Comparison of the displacement field for the resolved (a) and the first-order computational homogenization (b) plate model under axial tension.

TAB 3. Comparison of the resolved model with the homogenized IGA model under axial tension. Strains according to Eq. (13) in 10^{-3}, Δ is the deviation from the resolved model.

	Resolved	CLT-RVE	Δ %
DOFs	7 083 614	75	–
$\bar{\varepsilon}_{xx}$	1.9191	2.2368	+16.6
$\bar{\varepsilon}_{yy}$	0.2250	0.4100	+82.2
ν_{eff}	−0.1173	−0.1833	+56.3

3.2.2. In-Plane Shear

For the comparison under shear load, both models suppress the out-of-plane displacement u_z along all four edges, and two corner points are pinned in plane to remove the remaining rigid-body motion. The shear resultant of $N_{xy} = 105\,\text{N/mm}$ is applied as an edge load q so that the load is self-equilibrated and each edge carries a total force of $52.5\,\text{kN}$.

Fig. 6 shows the displacement field comparison. As already seen for the axial case, the first-order homogenization is too compliant. The effective shear strain in Tab. 4 was evaluated as a pair of central differences between the four mid-edge points of the plate, denoted by the superscripts t, b, r and l for the upper, lower, right and left mid-edge point,

$$\gamma_{xy} = \frac{u_x^{\mathrm{t}} - u_x^{\mathrm{b}}}{L_y} + \frac{u_y^{\mathrm{r}} - u_y^{\mathrm{l}}}{L_x},$$
$$A_{66,\text{eff}} = \frac{N_{xy}}{\gamma_{xy}}, \tag{14}$$

so that the two terms of γ_{xy} are the discrete counterparts of $\partial u_x/\partial y$ and $\partial u_y/\partial x$. For the IGA model, the effective shear stiffness $A_{66,\text{eff}}$ matches the A_{66} entry of the ABD matrix in Fig. 4.

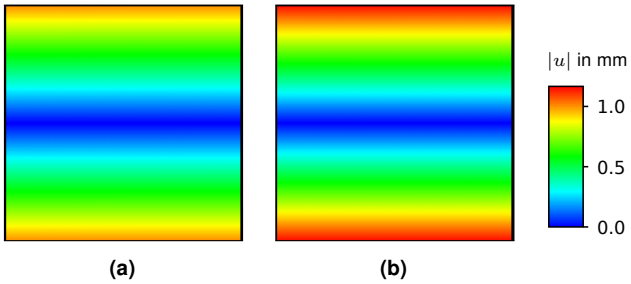


FIG 6. Comparison of the displacement field for the resolved (a) and the first-order computational homogenization (b) plate model under shear.

TAB 4. Shear, $N_{xy} = 105\,\text{N/mm}$. γ_{xy} in 10^{-3}, $A_{66,\text{eff}}$ in N/mm, Δ is the deviation from the resolved model.

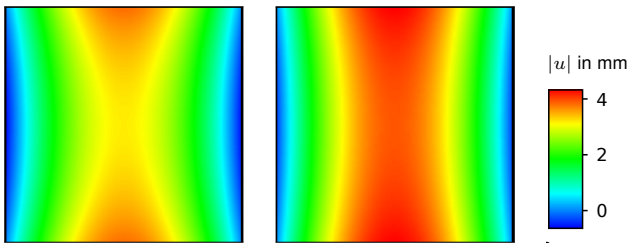
	Resolved	CLT-RVE	Δ %
DOFs	7 083 614	75	–
γ_{xy}	4.0383	4.6646	+15.5
$A_{66,\text{eff}}$	26 001	22 510	−13.4

3.2.3. Pure Bending

Pure bending is applied to the free plate with opposite moments of $M = 10^5\,\text{N mm}$ at the two ends, and three corner pins on the outer face remove the rigid-body motion in both models. In the resolved model, each full-thickness end set is coupled to a reference point that carries the moment. Since the Kirchhoff–Love shells of the IGA model have no rotational degrees of freedom, the same couple is introduced there as work-conjugate nodal loads on the control points of each end row.

Fig. 7 shows the comparison of the resolved and homogenized simulations. The curvatures in Tab. 5 were obtained by fitting a paraboloid to the out-of-plane displacement field by least squares, and the bending Poisson's ratio follows as $\nu_{\text{bending}} = -\kappa_{22}/\kappa_{11}$. Since the lateral edges are moment-free, it approximately reproduces the ratio D_{12}/D_{22} of the corresponding ABD matrix in Fig. 4. The first-order homogenization is again too compliant, overestimating κ_{11} by 12.6% and underestimating ν_{bending} by 48.4%.

CC BY 4.0



(a) (b)

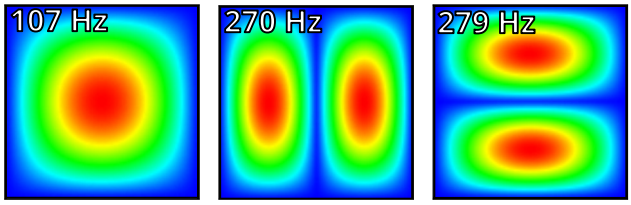
FIG 7. Comparison of the displacement field for the resolved (a) and the first-order computational homogenization (b) plate model under bending.

TAB 5. Bending, $M = 10^5$ N mm. Curvatures in 10^{-4}/mm, Δ is the deviation from the resolved model.

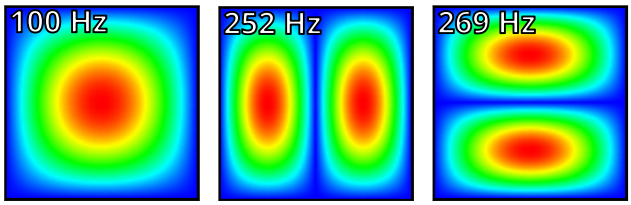
	Resolved	CLT-RVE	Δ %
DOFs	7 083 614	75	–
κ_{11}	1.2148	1.3684	+12.6
κ_{22}	−0.2041	−0.1186	−41.9
ν_{bending}	0.1681	0.0867	−48.4

3.2.4. Modal Analysis

For the modal analysis, the plate is simply supported along all edges, with two points pinned in plane to remove the remaining rigid-body motion. To account for higher modes, the homogenized model was refined to 1200 degrees of freedom. Fig. 8 compares the first three bending mode shapes and Tab. 6 the corresponding frequencies, where the in-plane modes of the resolved model are omitted. The first-order homogenization is again too compliant and therefore underestimates the frequencies by up to 6.6%.



(a) Resolved model



(b) First-order computational homogenization

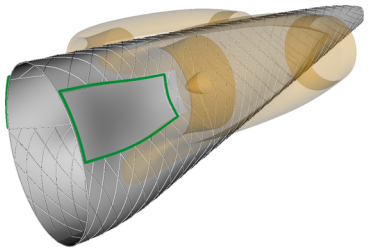
FIG 8. Comparison of the first three bending mode shapes for the resolved (a) and the first-order computational homogenization (b) plate model.

TAB 6. First three bending modes in Hz, Δ is the deviation from the resolved model.

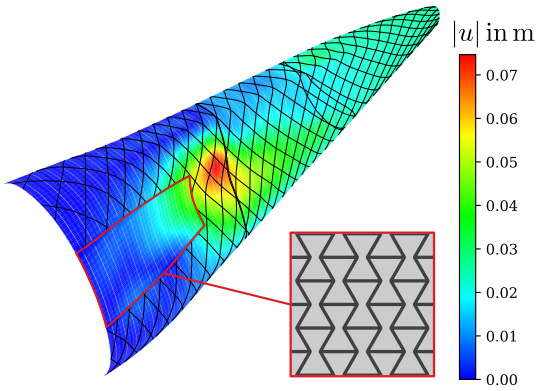
	Resolved	CLT-RVE	Δ %
DOFs	7 083 614	1200	–
Mode (1,1)	107.0	100.4	−6.2
Mode (2,1)	269.6	251.7	−6.6
Mode (1,2)	278.6	269.2	−3.4

4. APPLICATION TO THE STRUCTURAL ANALYSIS OF A REAR FUSELAGE SECTION

To demonstrate the complete scale-bridging workflow, the homogenized shell stiffnesses are assigned to the skin of a rear fuselage section, which is then analyzed with isogeometric analysis. Fig. 9a shows, as an example, the skin region to which the homogenized auxetic sandwich properties are assigned, and Fig. 9b the resulting displacement field for a 2.5 g pull-up maneuver. In this way, the structural behavior of the rear fuselage section can in future be tailored not only by changing the stiffener topology but also by changing the topology of the auxetic sandwich core cell.



(a) Skin region (green) to which the homogenized auxetic sandwich properties are assigned.



(b) Displacement magnitude $|u|$ of the rear fuselage section for a 2.5 g pull-up maneuver.

FIG 9. Application of the homogenized auxetic sandwich in the isogeometric analysis of the rear fuselage section.

5. SUMMARY AND OUTLOOK

The aim of this work is to make use of the advantages of auxetic metamaterials, such as passive vibration damping, high energy dissipation and the ability to tai-

CC BY 4.0

lor the deformation behavior, as the core material in sandwich structures. This could be particularly beneficial for the integration of engines into the fuselage for BLI configurations. However, a resolved simulation of the sandwich material is not feasible in this context.
A first-order homogenization of the core material was investigated to determine the homogenized shell stiffnesses of auxetic sandwich materials, whereby the core is treated as a laminate layer and the ABD matrices are determined using classical laminate theory. A resolved and a homogenized plate model were compared under tension, shear and bending as well as in a modal analysis. The homogenized model reproduces the deformation modes of the resolved plate, but is too compliant, with deviations of up to 82% in the transverse strain response. The scale-bridging workflow was demonstrated by assigning the homogenized stiffnesses to the inlet region of an isogeometric rear fuselage model and analyzing a $2.5\,\mathrm{g}$ pull-up maneuver.
In the future, an asymptotic homogenization of the complete sandwich section will be investigated, which avoids the plane-stress reduction and the separate treatment of core and faces of the present approach.

ACKNOWLEDGEMENTS

This work was funded by the Deutsche Forschungsgemeinschaft (DFG, German Research Foundation) – Project-ID 498601949 – TRR 364 (SynTrac, Project B06).

Contact address:

maximilian.friedrichs-dachale@tu-braunschweig.de

References

[1] Nicolas G. M. Moirou, Drewan S. Sanders, and Panagiotis Laskaridis. Advancements and prospects of boundary layer ingestion propulsion concepts. *Progress in Aerospace Sciences*, 138:100897, 2023. DOI: 10.1016/j.paerosci.2023.100897.

[2] Shishir A. Pandya, Alejandra Uranga, Alejandro Espitia, and Arthur Huang. Computational assessment of the boundary layer ingesting nacelle design of the D8 aircraft. In *52nd AIAA Aerospace Sciences Meeting*, National Harbor, MD, USA, 2014. AIAA Paper 2014-0907. DOI: 10.2514/6.2014-0907.

[3] Jan Hartmann and Stephan Staudacher. Engine–airframe integration — from Froude theorem to numerical flow simulation. *Engineering Proceedings*, 133(1):151, 2026. DOI: 10.3390/engproc2026133151.

[4] Yi Chao Qu, Xing Chi Teng, Yi Zhang, Wei Zhong Jiang, Meng Li Xue, Tao Xue, Jun Wen Shi, and Xin Ren. A novel 3D composite auxetic sandwich panel for energy absorption improvement. *Engineering Structures*, 322:119129, 2025. DOI: 10.1016/j.engstruct.2024.119129.

[5] Jia Shuo Liu, Yi Zhang, Xiang Jie Wei, Zhu Kun Mi, Tao Ding, Jia Hui Zhang, Tong Cheng, Lin Hua, Xin Guo, Kai Hao Lin, et al. Four-point bending behavior of auxetic sandwich structures. *Thin-Walled Structures*, 227:114954, 2026. DOI: 10.1016/j.tws.2026.114954.

[6] Luca Boldrin, S. Hummel, Fabrizio Scarpa, Dario Di Maio, Cristian Lira, Massimo Ruzzene, Chrystel D. L. Remillat, Teik-Cheng Lim, Ramesh Rajasekaran, and Sophoclis Patsias. Dynamic behaviour of auxetic gradient composite hexagonal honeycombs. *Composite Structures*, 149:114–124, 2016. DOI: 10.1016/j.compstruct.2016.03.044.

[7] Matheus Brendon Francisco, João Luiz Junho Pereira, Guilherme Antônio Oliver, Lucas Ramon Roque da Silva, Sebastião Simões Cunha Jr., and Guilherme Ferreira Gomes. A review on the energy absorption response and structural applications of auxetic structures. *Mechanics of Advanced Materials and Structures*, 29(27):5823–5842, 2022. DOI: 10.1080/15376494.2021.1966143.

[8] Nicolas Grünfelder, Maximilian Brodbeck, Navina Waschinsky, Tim Ricken, and Seyed Morteza Seyedpour. Puzzle-like auxetic lattice architectures employing dovetail joints: Experimental investigation of the structural dynamic behaviour. *Materials & Design*, 268:116408, 2026. DOI: 10.1016/j.matdes.2026.116408.

[9] Václav Nežerka, Michael Somr, Tomáš Janda, Jan Vorel, Martin Doškář, Jan Antoš, Jan Zeman, and Jan Novák. A jigsaw puzzle metamaterial concept. *Composite Structures*, 202:1275–1279, 2018. DOI: 10.1016/j.compstruct.2018.06.015.

[10] Kazuki Hayashi and Romain Mesnil. Multi-layer auxetic surfaces with compliant mechanisms. *Engineering Structures*, 341:120752, 2025. DOI: 10.1016/j.engstruct.2025.120752.

[11] Ulrich Kling, Arne Seitz, Julian Bijewitz, Andreas Hermanutz, Luiz da Rocha-Schmidt, Fabrizio Scarpa, Frane Majić, Gunilla Efraimsson, and Ciarán J. O'Reilly. Shape adaptive technology for aircraft engine nacelle inlets. In *Proceedings of the 5th Aircraft Structural Design Conference*. Royal Aeronautical Society, 2016.

[12] Sebastian W. Pattinson, Meghan E. Huber, Sanha Kim, Jongwoo Lee, Sarah Grunsfeld, Ricardo Roberts, Gregory Dreifus, Christoph Meier, Lei Liu, Neville Hogan, and A. John Hart. Additive manufacturing of biomechanically tailored meshes for compliant wearable and implantable devices. *Advanced Functional Materials*, 29(32):1901815, 2019. DOI: 10.1002/adfm.201901815.

[13] Nicolas Grünfelder, Manmit Padhy, Alaa Armiti-Juber, Seyed Morteza Seyedpour, Navina Waschinsky, and Tim Ricken. Reduced-order modeling of lattice structures through iterative beam fitting and static mesoscale projection. *Results in Engineering*, 27:106529, 2025. DOI: 10.1016/j.rineng.2025.106529.

[14] Chonghui Zhang and Yaoyao Fiona Zhao. A critical review on the application of machine learning in supporting auxetic metamaterial design. *Journal of Physics: Materials*, 7(2):022004, 2024. DOI: 10.1088/2515-7639/ad33a4.

[15] Alexander L. Kalamkarov, Igor V. Andrianov, and Vladyslav V. Danishevs'kyy. Asymptotic homogenization of composite materials and structures. *Applied Mechanics Reviews*, 62(3):030802, 2009. DOI: 10.1115/1.3090830.

[16] Albert Desmoulins and Dennis M. Kochmann. Local and nonlocal continuum modeling of inelastic periodic networks applied to stretching-dominated trusses. *Computer Methods in Applied Mechanics and Engineering*, 313:85–105, 2017. DOI: 10.1016/j.cma.2016.09.027.

[17] A. S. Kaddour and M. J. Hinton. Input data for test cases used in benchmarking triaxial failure theories of composites. *Journal of Composite Materials*, 46(19–20):2295–2312, 2012. DOI: 10.1177/0021998312449886.

[18] J. Austin Cottrell, Thomas J. R. Hughes, and Yuri Bazilevs. *Isogeometric Analysis: Toward Integration of CAD and FEA*. Wiley, Chichester, UK, 2009. ISBN: 978-0-470-74873-2. DOI: 10.1002/9780470749081.

[19] Kay Sommerwerk. *Isogeometrische Analyse für die Optimierung von Leichtbaustrukturen im Flugzeugbau*. PhD thesis, Technische Universität Braunschweig, Braunschweig, Germany, 2017. Forschungsbericht 2017-04, Niedersächsisches Forschungszentrum für Luftfahrt.

[20] Anna M. Bauer, Michael Breitenberger, Benedikt Philipp, Roland Wüchner, and Kai-Uwe Bletzinger. Embedded

CC BY 4.0

structural entities in NURBS-based isogeometric analysis. *Computer Methods in Applied Mechanics and Engineering*, 325:198–218, 2017. DOI: 10.1016/j.cma.2017.07.010.

[21] Vicente Mataix Ferrándiz et al. KratosMultiphysics/Kratos: Release v10.2.3. Zenodo, 2025. DOI: 10.5281/zenodo.15687676.

CC BY 4.0